A spectral–fundamental solution approach for fully nonlinear ship wave simulations

Kaiyuan Shi,[1,2] Renchuan Zhu,[1,*] and Yulong Li[3]

[1] *State Key Laboratory of Ocean Engineering, Shanghai Jiao Tong University, Shanghai 200240, China*

[2] *Hainan Research Institute, Shanghai Jiao Tong University, Hainan 572024, China*

[3] *Technology Centre for Offshore and Marine, Singapore (TCOMS), Singapore 118411, Singapore*

(Dated: March 18, 2026)

This study presents a novel spectral–fundamental solution (SFS) method which enables efficient simulation of large-scale nonlinear wave–body interactions. The SFS method combines spectral basis functions and fundamental solutions to achieve both global efficiency and local accuracy. Based on the linearity of the Laplace equation, it decomposes large-scale boundary-value problems into independent subproblems, enabling efficient full-domain computation. Numerical validations show that SFS achieves higher accuracy than the high-order spectral method for short, steep waves and outperforms the method of fundamental solutions in long-wave conditions. Applications to nonlinear ship waves in large-scale domains yield results in good agreement with experimental data, successfully capturing higher-order nonlinear effects. The simulations reveal the physical origins of distinct energy bands in the wave spectrogram and demonstrate how ship acceleration influences the ship-generated wake field. Furthermore, the simulations explain why high-speed ships exhibit wake angles narrower than classical predictions. Beyond ship waves, this efficient SFS framework can be extended to a wide range of unsteady wave–structure interaction problems in ocean engineering.

I. INTRODUCTION

As ships move through water, they generate striking V-shaped wakes that reveal complex interactions between the vessel and the free surface. Unlike ordinary water waves, ship wakes are confined within a well-defined wedge angle, and their geometric patterns remain clearly visible even kilometers away. The persistent propagation of these waves presents notable engineering and environmental concerns. Repeated wake impacts accelerate shoreline erosion and disrupt coastal ecosystems [1–3]. In busy waterways, overlapping wakes from multiple vessels can create complex wave fields that pose risks to navigational safety [4, 5]. Within port environments, wake-induced motions may cause excessive movement of moored ships and even cause damage to berthing facilities [6, 7]. Therefore, a comprehensive understanding of the large-scale propagation of ship wakes is essential for effective waterway management, minimizing environmental impacts, and maintaining maritime safety.

Ship waves represent a classic example of nonlinear wave–structure interaction. As a ship moves forward and displaces water, it generates steep, strongly nonlinear surface gravity waves in the near field. As these waves propagate outward, their evolution becomes increasingly complex due to both dispersive effects and nonlinear interactions among waves,

* Contact author: renchuan@sjtu.edu.cn

which pose significant challenges for analysis and prediction. The theoretical study of ship waves dates back to the pioneering work of Lord Kelvin [8]. By assuming inviscid, irrotational potential flow and linearizing the free-surface boundary condition, Kelvin applied the stationary phase method to characterize the steady wake pattern generated by a moving point disturbance. Within this idealized framework, the free surface behaves as a linear system: waves radiate outward according to the linear dispersion relation and do not interact with one another. Building on this foundation, subsequent researchers developed simplified ship models to facilitate analysis. Notable examples include *thin ships* with negligible beam [9, 10] and *flat ships* with vanishing draft [11, 12]. These models have produced a variety of semi-analytical solutions, further advancing the understanding of ship-generated wave patterns.

Linear ship wave theory was further advanced by the Neumann–Kelvin (N–K) approach [13], which employs Green's functions. In the N–K framework, Kelvin sources that satisfy the linear free-surface condition are distributed along the hull, producing a wave field that meets both the hull's impermeability and the linear free-surface boundary conditions. Later, Noblesse *et al.* [14] addressed inconsistencies in the treatment of the waterline within N–K theory and introduced the Neumann–Michell theory. These linear models have proven effective in explaining phenomena such as the wake angle of high-speed vessels [15–17] and some spectrogram features of wave heights at observation points [18–20]. However, neglecting nonlinear effects restricts the capacity of these models to accurately characterize ship-generated wave fields.

To address nonlinear ship wave problems, the boundary element method (BEM) is widely used for potential flow simulations [21–23]. BEM discretizes both the nonlinear free surface and the wetted hull, updating boundary positions iteratively or through time-stepping to resolve the nonlinear wave field. While this method requires discretization only of flow boundaries, it necessitates constructing dense matrices and solving large linear systems. Even with iterative solvers, the computational complexity remains $O(N^2)$, posing challenges for simulations over large domains. To enhance computational efficiency, techniques such as the fast multipole method [24] and pre-corrected Fast Fourier Transform [25, 26] have been introduced to reduce the burden of dense matrix operations. Alternatively, some researchers have adopted spatial discretization methods, which trade increased degrees of freedom for sparse matrices and more manageable linear systems [27–30].

In addition, finite volume methods (FVM) for solving the Navier–Stokes equations [31–33] are widely used to simulate near-field ship wave flows. These viscous flow approaches discretize the entire flow domain and leverage methods such as VOF or Level-Set to capture the air–water interface, enabling effective simulation of viscous effects and strongly nonlinear phenomena like wave breaking. However, viscous approaches demand very fine grids and consequently incur high computational costs; moreover, they are susceptible to numerical dissipation that may reduce the accuracy of far-field wave results.

Although numerical methods for near-field simulations are well established, significant challenges remain in modeling the far-field nonlinear characteristics of ship wakes. The wake produced by a moving vessel can extend for kilometers, requiring computational domains that span dozens of ship lengths to accurately capture far-field effects. Since the characteristic wavelength of ship-generated waves is only a fraction of the ship length, BEM may require nearly a million surface elements, while FVM could demand up to a hundred million volume cells. This enormous computational load makes large-scale nonlinear wave–structure interaction simulations impractical with conventional techniques. To address these challenges, a common simplification is to model the hull as a submerged body or a mov-

ing pressure source. This approach eliminates direct intersection between the hull and the free surface, allowing the free surface to be represented on a uniform grid and enabling computational resources to focus on nonlinear wave dynamics. For example, Forbes [34] combined Green's second identity with Newton's method to solve the nonlinear system, establishing a framework for steady nonlinear ship wave computation. Building on this, Pethiyagoda *et al.* [35] introduced the Jacobian-free Newton–Krylov (JFNK) method and leveraged graphics processing unit (GPU) acceleration to achieve substantial computational gains. Subsequently, Pethiyagoda *et al.* [36] employed the JFNK method to connect multiple computational subdomains, successfully simulating steady nonlinear ship waves induced by a pressure source on a 1625×551 grid. In this work, second-order nonlinear effects in ship wake spectrograms were, for the first time, successfully reproduced numerically. However, the pressure source model is most effective for shallow-draft vessels and cases with weak nonlinearities. The nonlinear and unsteady characteristics of displacement-type ships remain an important area for further investigation.

To advance the study of large-scale nonlinear characteristics of ship wakes, it is essential to overcome the efficiency and accuracy limitations of existing methods for nonlinear wave–structure interaction simulations. In this paper, we introduce an efficient spectral–fundamental solution (SFS) method[37]. The SFS approach combines a high-order spectral (HOS) method for nonlinear wave propagation within the computational domain with fundamental solutions near the hull to accurately capture local flow features. By integrating the global efficiency of pseudo-spectral techniques with the local adaptability of the method of fundamental solutions (MFS), the SFS method enables precise simulation of nonlinear wave–structure interactions and far-field wave dynamics across large computational domains with minimal computational cost.

Using this approach, we have successfully simulated nonlinear ship waves generated by a displacement vessel in an ultra-large domain of 4096×4096 grids. The resulting wave patterns exhibit pronounced higher-order nonlinear features and spectral components that closely align with experimental observations. Furthermore, we provide a detailed analysis of the spectrogram characteristics of nonlinear ship wakes and elucidate several features observed in measured spectrograms.

The remainder of this paper is organized as follows: Section II presents the governing equations and boundary conditions for simulating nonlinear wave–structure interactions. Section III introduces the SFS method, outlining the core concepts and comparing its accuracy with HOS and MFS approaches. In Section IV, we first validate the SFS results against benchmark experiments, and then present large-scale nonlinear ship wave simulations to discuss the spatial and spectrogram characteristics of nonlinear ship wakes. Finally, Section V provides concluding remarks.

II. MATHEMATICAL MODEL OF THE SHIP WAVE PROBLEM

A. Governing equations

Consider a vessel advancing in an infinitely deep ocean. We use a Cartesian coordinate system with the z-axis pointing vertically upward, where $z = 0$ defines the still water surface. The water is treated as an incompressible, homogeneous, inviscid fluid. For irrotational flow, a velocity potential ϕ exists such that its gradient yields the fluid velocity. By the continuity

equation, ϕ satisfies the Laplace equation:

$$\nabla\phi = (u, v, w), \tag{1a}$$

$$\nabla^2\phi = \nabla \cdot (u, v, w) = 0. \tag{1b}$$

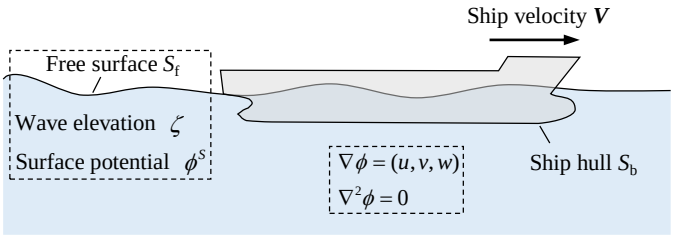

FIG. 1. Nonlinear wave-making problem for a moving ship. The flow field is represented by velocity potential ϕ, with boundaries comprising the free surface S_f and the ship hull S_b.

The fluid domain is bounded by the free surface S_f and the wetted hull surface S_b. The primary variables of interest are the wave elevation $\zeta(x, y, t)$ generated by the ship and the free-surface velocity potential $\phi^S(x, y, t) = \phi(x, y, \zeta, t)$. As illustrated in Fig. 1, when the ship starts from rest and moves with a prescribed velocity, the governing initial boundary value problem can be formulated as follows[38]:

$$\begin{cases} \nabla^2\phi = 0 & \text{in the fluid domain} \\ \zeta_t = (1 + |\nabla_{\boldsymbol{x}}\zeta|^2)\phi_z - \nabla_{\boldsymbol{x}}\phi^S \cdot \nabla_{\boldsymbol{x}}\zeta & \text{on } S_f \\ \phi_t^S = -g\zeta - \dfrac{1}{2}|\nabla_{\boldsymbol{x}}\phi^S|^2 + \dfrac{1}{2}(1 + |\nabla_{\boldsymbol{x}}\zeta|^2)\phi_z^2 & \text{on } S_f \\ \phi_n = \boldsymbol{V} \cdot \boldsymbol{n} & \text{on } S_b \\ \nabla\phi \to 0 & \text{as } z \to -\infty \\ \phi = 0, \zeta = 0 & \text{at } t = 0 \end{cases}. \tag{2}$$

Here, g denotes gravitational acceleration, and $\nabla_{\boldsymbol{x}} \equiv (\partial/\partial x, \partial/\partial y)$ is the horizontal gradient operator. $\boldsymbol{V}$ is the prescribed ship velocity, and $\boldsymbol{n}$ is the unit normal vector to the hull surface.

While the free surface boundary S_f in Eq. (2) are theoretically unbounded, practical numerical simulations require truncating the computational domain. To prevent undesired wave reflections at the boundaries, a damping procedure is applied at each time step to gradually reduce ζ and ϕ^S to zero near the boundaries:

$$\begin{aligned} \zeta' &= \alpha\zeta, \\ \phi^{S\prime} &= \alpha\phi^S, \end{aligned} \tag{3}$$

where α is a relaxation function that transitions smoothly from 0 at the domain boundary to 1 within the interior:

$$\alpha = \begin{cases} \sin^2\left(\dfrac{\pi}{2}\dfrac{d_r}{l_r}\right) & \text{if } d_r/l_r < 1 \\ 1 & \text{if } d_r/l_r \geq 1 \end{cases}. \tag{4}$$

Here, d_r is the shortest distance to the truncated boundary, and l_r is the width of the relaxation zone, set to twice the characteristic wavelength in this study.

B. Time-domain wave evolution

In this study, the initial boundary value problem defined by Eq. (2) is integrated forward in time using a fourth-order Runge–Kutta scheme. At each time step, the current values of ζ and ϕ^S are known, and their time derivatives, ζ_t and ϕ_t^S, are computed on the free surface $\mathrm{S_f}$ according to Eq. (2). The spatial derivatives $\nabla_{\boldsymbol{x}}\zeta$ and $\nabla_{\boldsymbol{x}}\phi^S$ that appear in these equations can be efficiently evaluated using finite difference methods or similar approaches. However, determining ϕ_z on $\mathrm{S_f}$ requires solving the following boundary value problem:

$$\begin{cases} \nabla^2\phi = 0 & \text{in the fluid domain} \\ \phi = \phi^S & \text{on } \mathrm{S_f} \\ \phi_n = \boldsymbol{V}\cdot\boldsymbol{n} & \text{on } \mathrm{S_b} \\ \nabla\phi \to 0 & \text{as } z \to -\infty \end{cases}. \tag{5}$$

As a nonlinear problem, the shapes of both the free surface $\mathrm{S_f}$ and the wetted hull surface $\mathrm{S_b}$ evolve over time. In conventional BEMs, the coefficient matrix must be reconstructed at every time step to reflect the updated geometry and to solve the mixed Dirichlet–Neumann boundary conditions in Eq. (5). As a result, the matrices cannot be reused between time steps, and each step involves assembling and solving a dense $N \times N$ matrix, resulting in a computational complexity of $O(N^3)$.

To overcome this limitation, we introduce the SFS method, which enables efficient solution of the boundary value problem described by Eq. (5).

III. SPECTRAL–FUNDAMENTAL SOLUTION (SFS) METHOD

A. Numerical discretization

The boundary discretization used in this study is illustrated in Fig. 2. The boundaries of the computational domain are represented by three distinct components: a uniformly spaced grid, a set of scattered points on the free surface, and triangular surface elements on the ship hull. The uniformly spaced grid, referred to as the *spectral layer*, serves as the collocation points for the Fourier pseudo-spectral method and covers the entire domain, comprising a total of N_s nodes. The N_f free-surface source points and N_b body surface elements are concentrated in the near-field region, functioning as source points or panels for the method of fundamental solutions. The rectangular region containing these free-surface sources and collocation points is termed the *fundamental solution domain*.

To avoid singularities in the flow field, each free-surface source point is placed above its corresponding collocation point on the free surface by a distance Δz, thereby eliminating the singularity of the source point within the fluid domain. This approach is commonly referred to as the *desingularized source method*. Cao *et al.* [39] performed a detailed analysis and showed that increasing Δz within a reasonable range can improve the accuracy of wave simulations, but also increases the condition number of the system matrix. In the present study, Δz is set equal to one horizontal grid spacing.

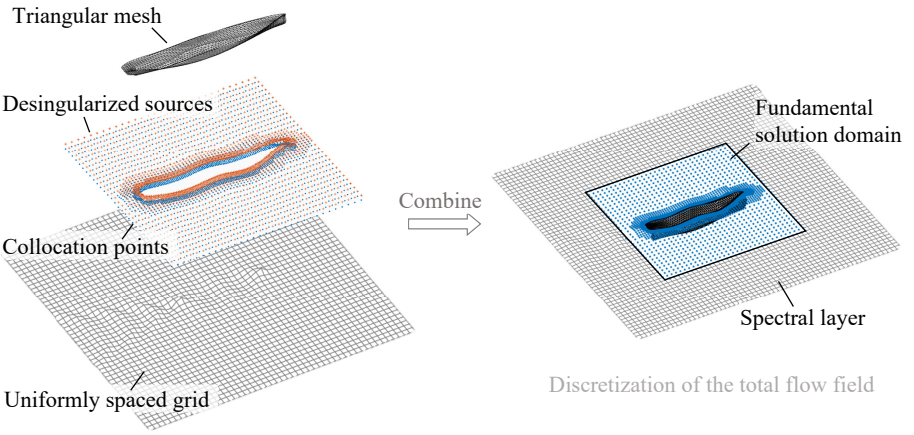

FIG. 2. Numerical discretization of the flow field boundary.

For a collocation point on the free surface at (ξ, η, ζ), the corresponding source point is located at $(\xi, \eta, \zeta + \Delta z)$, and the induced velocity potential at a field point (x, y, z) is given by

$$F(x, y, z) = \frac{1}{\sqrt{(x-\xi)^2 + (y-\eta)^2 + (z-\zeta-\Delta z)^2}}. \tag{6}$$

For each triangular body panel, singular $1/r$ sources are distributed uniformly with equal strength across the panel, with its geometric center serving as the collocation point in the calculations. For a triangular panel with constant source strength, the induced velocity potential at a field point (x, y, z) is

$$\begin{aligned} F^{\text{tri}}(x, y, z) &= \int_{\text{tri}} F(x, y, z) - F^{\text{mirror}}(x, y, z)\, dS \\ &= \int_{\text{tri}} \frac{1}{\sqrt{(x-\xi)^2 + (y-\eta)^2 + (z-\zeta)^2}}\, dS \\ &- \int_{\text{tri}} \frac{1}{\sqrt{(x-\xi)^2 + (y-\eta)^2 + (z+\zeta+2\delta)^2}}\, dS, \end{aligned} \tag{7}$$

where the subscript "tri" denotes integration over the triangular panel, and (ξ, η, ζ) denotes the coordinates of the source distributed over the panel. Unlike the point source in Eq. (6), Eq. (7) includes an additional mirror source with respect to the plane $z = \delta$ for numerical convenience; here, δ is defined as the maximum elevation of the free surface.

B. Decomposition strategy

In the SFS method, the velocity potential ϕ within the flow domain is decomposed into two components: one represented by spectral basis functions and the other by fundamental

solutions,

$$\phi(\boldsymbol{x}, z) = \phi^{\text{spec}}(\boldsymbol{x}, z) + \phi^{\text{fund}}(\boldsymbol{x}, z), \tag{8}$$

where

$$\begin{aligned} \phi^{\text{spec}}(\boldsymbol{x}, z) &= \Re\left(\sum_j A_j S_j(\boldsymbol{x}, z)\right), \\ \phi^{\text{fund}}(\boldsymbol{x}, z) &= \sum_j \sigma_j F_j(\boldsymbol{x}, z). \end{aligned} \tag{9}$$

Here, $\Re(\cdot)$ denotes the real part. S_j and A_j are the basis functions and their complex amplitudes in the pseudo-spectral method, respectively, while F_j and σ_j are the fundamental solutions and their source strengths. For the case of infinite water depth considered in this work, the basis function S_j in the pseudo-spectral method is defined as

$$S_j(\boldsymbol{x}, z) = e^{|\boldsymbol{k}_j| z + \mathrm{i}\boldsymbol{k}_j \cdot \boldsymbol{x}}, \tag{10}$$

where $\boldsymbol{x} \equiv (x, y)$ is the horizontal position vector, $\boldsymbol{k}_j \equiv (k_{jx}, k_{jy})$ is the wavenumber vector, and $|\boldsymbol{k}_j|$ its magnitude.

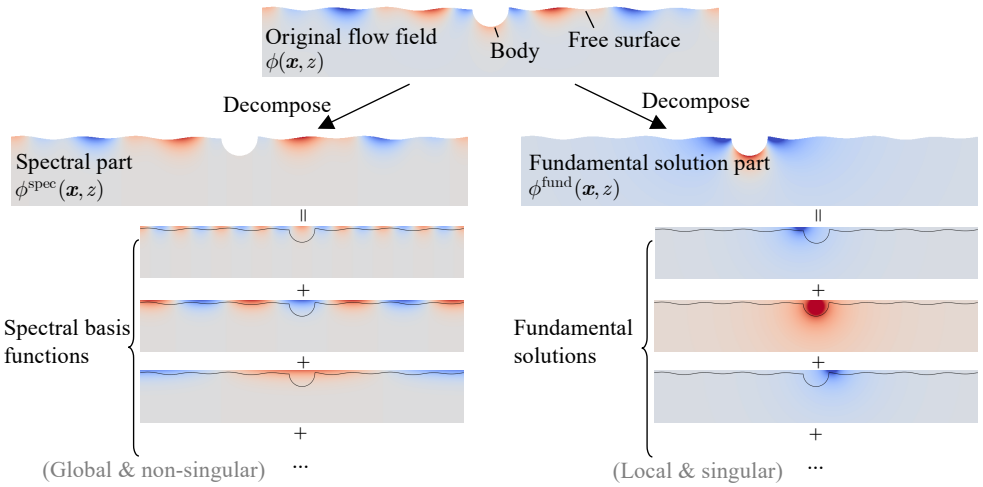

FIG. 3. Schematic of the spectral–fundamental solution method.

For a uniform grid with N_s collocation points, the basis functions S_j form N_s independent modes, each associated with a complex amplitude. These amplitudes collectively form the unknown vector $\boldsymbol{s}$. Given $\boldsymbol{s}$, the velocity potential on any z-plane can be efficiently evaluated on the grid using the Fast Fourier Transform (FFT). Interpolation methods can then be applied to calculate the velocity potential and velocity field at arbitrary locations. In this work, two linear operators are introduced: $\mathcal{M}^\text{f}$ maps $\boldsymbol{s}$ to the free-surface velocity potential, and $\mathcal{M}^\text{b}$ maps $\boldsymbol{s}$ to the normal velocity on the body surface. Both operations have computational complexity $O(N_\text{s} \log N_\text{s})$.

Similarly, the source strengths for the N_f free-surface point sources and N_b body surface panels are represented by vectors $\boldsymbol{\sigma}_\mathrm{f}$ and $\boldsymbol{\sigma}_\mathrm{b}$, respectively. The linear operators $\mathcal{L}^\mathrm{f}$ and $\mathcal{L}^\mathrm{b}$ describe the contributions of the fundamental solutions to the free-surface velocity potential and the normal velocity on the body surface.

By construction, the linear combination of fundamental solutions and basis functions for ϕ inherently satisfies the Laplace equation and the bottom boundary condition as $z \to -\infty$. The remaining task is to determine the coefficients of these components so that their sum satisfies the Dirichlet condition on the free surface $\mathrm{S_f}$ and the Neumann condition on the hull surface $\mathrm{S_b}$, as required by Eq. (5):

$$\begin{cases} \mathcal{L}^\mathrm{f}_\mathrm{f}\boldsymbol{\sigma}_\mathrm{f} + \mathcal{L}^\mathrm{f}_\mathrm{b}\boldsymbol{\sigma}_\mathrm{b} + \mathcal{M}^\mathrm{f}\boldsymbol{s} = \phi^S \\ \mathcal{L}^\mathrm{b}_\mathrm{f}\boldsymbol{\sigma}_\mathrm{f} + \mathcal{L}^\mathrm{b}_\mathrm{b}\boldsymbol{\sigma}_\mathrm{b} + \mathcal{M}^\mathrm{b}\boldsymbol{s} = \boldsymbol{V}\cdot\boldsymbol{n} \end{cases}. \tag{11}$$

The core of the SFS method lies in efficiently solving for $\boldsymbol{\sigma}$ and $\boldsymbol{s}$ such that Eq. (11) is satisfied. Once the source strengths and modal amplitudes are determined, the vertical velocity ϕ_z on the free surface $\mathrm{S_f}$ can be computed as

$$\begin{aligned} \phi_z(\boldsymbol{x},\zeta) &= \phi_z^\mathrm{spec}(\boldsymbol{x},\zeta) + \phi_z^\mathrm{fund}(\boldsymbol{x},\zeta) \\ &= \Re\left(\sum_j A_j \frac{\partial}{\partial z} S_j(\boldsymbol{x},\zeta)\right) + \sum_j \sigma_j \frac{\partial}{\partial z} F_j(\boldsymbol{x},\zeta). \end{aligned} \tag{12}$$

C. Solution procedure of SFS

The SFS method solves the source strengths and modal amplitudes that satisfy Eq. (11) through the following stepwise procedure:

$$W\ \mathcal{L}^\mathrm{f}_\mathrm{f}\, W\boldsymbol{\sigma}_\mathrm{f1} = \phi^S, \tag{13a}$$

$$\mathcal{M}^\mathrm{f}\boldsymbol{s} = \phi^S - \mathcal{L}^\mathrm{f}_\mathrm{f}\boldsymbol{\sigma}_\mathrm{f1}, \tag{13b}$$

$$\begin{bmatrix} \mathcal{L}^\mathrm{f}_\mathrm{f} & \mathcal{L}^\mathrm{f}_\mathrm{b} \\ \mathcal{L}^\mathrm{b}_\mathrm{f} & \mathcal{L}^\mathrm{b}_\mathrm{b} \end{bmatrix} \begin{bmatrix} \boldsymbol{\sigma}_\mathrm{f2} \\ \boldsymbol{\sigma}_\mathrm{b} \end{bmatrix} = \begin{bmatrix} 0 \\ \boldsymbol{V}\cdot\boldsymbol{n} - \mathcal{L}^\mathrm{b}_\mathrm{f}\boldsymbol{\sigma}_\mathrm{f1} - \mathcal{M}^\mathrm{b}\boldsymbol{s} \end{bmatrix}, \tag{13c}$$

$$\boldsymbol{\sigma}_\mathrm{f} = \boldsymbol{\sigma}_\mathrm{f1} + \boldsymbol{\sigma}_\mathrm{f2}. \tag{13d}$$

Here, W is a weight function defined within the fundamental solution domain:

$$W(x,y) = W_x(x,y)\cdot W_y(x,y), \tag{14a}$$

$$W_x(x,y) = \begin{cases} 1 & \text{if } d_x/l_w > 1 \\ (d_x/l_w - 1)^2 + 1 & \text{if } d_x/l_w \le 1 \end{cases}, \tag{14b}$$

$$W_y(x,y) = \begin{cases} 1 & \text{if } d_y/l_w > 1 \\ (d_y/l_w - 1)^2 + 1 & \text{if } d_y/l_w \le 1 \end{cases}. \tag{14c}$$

where l_w is the prescribed transition width of the weight function, and d_x, d_y are the shortest distances from a point in the fundamental solution domain to the nearest boundary along the x and y axes, respectively, as shown in Fig. 4.

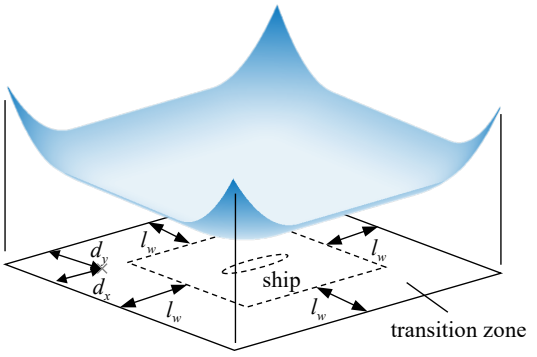

FIG. 4. Distribution of the weight function W within the fundamental solution domain.

In Eq. (13a), the solution for σ_{f1} involves only the collocation points on the free surface, which is inside the fundamental solution domain. The operator $\mathcal{L}_{\mathrm{f}}^{\mathrm{f}}$ is an $N_{\mathrm{f}} \times N_{\mathrm{f}}$ matrix, and the resulting linear system in Eq. (13a) is solved iteratively using the Generalized Minimum Residual (GMRES) algorithm, yielding a computational complexity of $O(N_{\mathrm{f}}^2)$.

Once $\boldsymbol{\sigma}_{\mathrm{f1}}$ is obtained, the velocity potential induced by the free surface sources can be evaluated at the spectral collocation points. To reduce the computational cost, this step is performed efficiently using the Barnes–Hut algorithm [40], which organizes the free-surface sources into a hierarchical quad-tree structure and approximates the far-field contributions of distant source groups, thereby avoiding the direct evaluation of all pairwise interactions. The resulting computational complexity is approximately $O(N_{\mathrm{s}} \log N_{\mathrm{f}})$.

The modal amplitudes for the spectral layer, $\boldsymbol{s}$, are then determined by solving Eq. (13b) using the HOS method [41]. The HOS method is a pseudo-spectral approach in which the velocity potential is expressed as a perturbation expansion and evaluated through Taylor series expansions on the free surface. By using FFT, the nonlinear Dirichlet problem on the free surface is solved efficiently with a computational complexity of $O(N_{\mathrm{s}} \log N_{\mathrm{s}})$, yielding the complex modal amplitudes of the velocity potential. It should be noted that, due to the intersection of the body and the free surface, a void exists on the free surface $\mathrm{S_f}$. As a result, the boundary values at spectral collocation points within this void on the right-hand side of Eq. (13b) are undefined. In practice, these undefined values are interpolated from neighboring spectral collocation points to ensure continuity and accuracy in the computation.

Finally, Eq. (13c) is solved for $\boldsymbol{\sigma}_{\mathrm{f2}}$ and $\boldsymbol{\sigma}_{\mathrm{b}}$. The purpose of $\boldsymbol{\sigma}_{\mathrm{f2}}$ is to counteract the velocity potential on the nonlinear free surface induced by $\boldsymbol{\sigma}_{\mathrm{b}}$. Since the panels on the body include mirror sources and act as dipoles, the velocity potential $\boldsymbol{\sigma}_{\mathrm{b}}$ induce on the free surface decays cubically with distance from the body. In the SFS method, the velocity potential induced by $\boldsymbol{\sigma}_{\mathrm{b}}$ in the far field, outside the fundamental solution domain, is considered negligible. Therefore, source points are not distributed beyond this region.

In particular, for the linear case where $\mathrm{S_f}$ remains the plane $z = 0$, symmetry dictates $F^{\mathrm{tri}}(x, y, 0) \equiv 0$, and thus $\mathcal{L}_{\mathrm{b}}^{\mathrm{f}} \boldsymbol{\sigma}_{\mathrm{b}} \equiv 0$. Eq. (13c) can then be simplified as follows:

$$\boldsymbol{\sigma}_{\mathrm{f2}} = 0, \tag{15a}$$

$$\mathcal{L}_{\mathrm{b}}^{\mathrm{b}} \boldsymbol{\sigma}_{\mathrm{b}} = \boldsymbol{V} \cdot \boldsymbol{n} - \mathcal{L}_{\mathrm{f}}^{\mathrm{b}} \boldsymbol{\sigma}_{\mathrm{f1}} - \mathcal{M}^{\mathrm{b}} \boldsymbol{s}. \tag{15b}$$

In summary, the SFS method avoids the direct solution of a large matrix system of size $N_{\mathrm{f}}+N_{\mathrm{b}}+N_{\mathrm{s}}$ by decomposing the original boundary value problem over a large computational domain into three smaller, tractable subproblems. The main flow field is efficiently captured by spectral basis functions and solved with $O(N_{\mathrm{s}} \log N_{\mathrm{s}})$ complexity, greatly reducing computational cost. Body surface panels address the pseudo-spectral method's limitations in representing underwater disturbances, while desingularized source points provide a detailed description of near-field flow features.

D. Algorithm Validation

1. *Dirichlet problem: nonlinear free-surface case without a body*

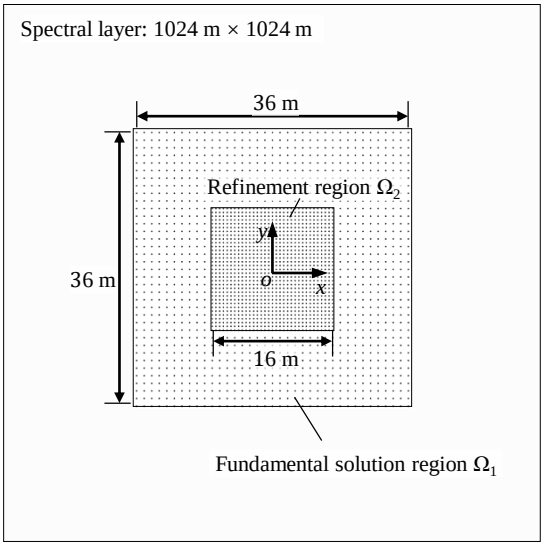

FIG. 5. Node arrangement in the computational domain.

To validate the proposed SFS method, we first conduct an error analysis for a scenario involving only the free surface, with no body present. Numerical experiments are performed in the computational domain shown in Fig. 5. The domain employs a 1024×1024 uniformly spaced grid as the background spectral layer, with a node spacing of 1 m and the origin located at the grid center. The fundamental solution region, denoted as Ω_1, is defined as the rectangle $(x, y) \in [-18, 18] \times [-18, 18]$. The weight function width, l_w, is set to 8 m. Within the refined region $(x, y) \in [-8, 8] \times [-8, 8]$, denoted as Ω_2, the node spacing is reduced to 0.5 m for increased resolution.

The following boundary conditions are specified throughout the domain:

$$\begin{aligned} \zeta(x, y) &= A\cos(kx), \\ \phi^S(x, y) &= A\sqrt{g/k}\exp(k\zeta)\sin(kx), \end{aligned} \tag{16}$$

where A is the wave amplitude, $k = 2\pi/\lambda$ is the wavenumber, and $\varepsilon = kA$ represents the degree of nonlinearity at the boundary. These conditions approximate regular surface gravity waves commonly observed in natural environments. The corresponding theoretical vertical velocity on the free surface is given by:

$$\phi_z(x, y, \zeta) = A\sqrt{gk}\exp(k\zeta)\sin(kx). \tag{17}$$

We test three different nonlinearity parameters: $\varepsilon_{1,2,3} = 0.005, 0.2, 0.4$. The HOS method, MFS, and the proposed SFS method are used to solve for these boundary conditions, and ϕ_z is computed within both Ω_1 and Ω_2. Results for the HOS method are obtained using the open-source *HOS-Ocean* code by Ducrozet et al. [42], with the grid configuration matching that of the spectral layer in the SFS method and a truncation order of three for the perturbation expansion. Since the HOS method is limited to uniform grids, node velocities in the refined region Ω_2 are calculated using FFT padding. For the MFS calculations, the setup matches the fundamental solution domain used in the SFS method. The L_2 relative error between numerical and theoretical solutions is reported for each method, with all errors for Ω_1 and Ω_2 summarized in Fig. 6 and Table I.

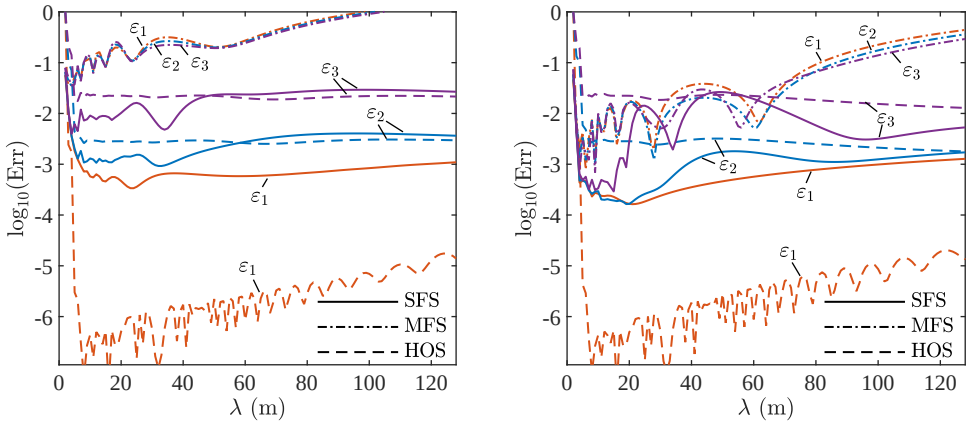

(a) L_2 relative error in region Ω_1 (b) L_2 relative error in region Ω_2

FIG. 6. Comparison of L_2 relative errors from different methods.

As shown in Fig. 6 and Table I, for nearly linear waves ($\varepsilon = 0.005$), within region Ω_1, the HOS method delivers the highest accuracy, while MFS yields the lowest accuracy. The SFS method produces intermediate results, with errors falling between those of HOS and MFS. As wave nonlinearity increases ($\varepsilon = 0.2, 0.4$), the error trend for MFS remains largely unchanged, but SFS maintains accuracy comparable to HOS and even slightly surpasses it for shorter wavelengths ($\lambda < 50\,\mathrm{m}$).

In the refined region Ω_2, both MFS and SFS demonstrate notable improvements in accuracy compared to Ω_1. While SFS remains less precise than the spectral method for nearly linear waves, it provides higher accuracy than HOS when nonlinearity is strong (ε_2 and ε_3). Similar to the results in Ω_1, MFS errors increase rapidly as wavelength grows.

Among the three methods considered, the HOS method employs a large computational domain covering $1024\,\mathrm{m} \times 1024\,\mathrm{m}$. However, as a perturbation approach relying on the low wave steepness assumption, its accuracy degrades when simulating strongly nonlinear

TABLE I. Comparison of L_2 relative errors in solving nonlinear free surfaces with various wave steepness and wavelengths using different methods.

			λ (m)						
			2	4	8	16	32	64	128
Ω_1	$\varepsilon = 0.005$	SFS	5.68×10^{-2}	3.61×10^{-3}	7.17×10^{-4}	5.14×10^{-4}	6.15×10^{-4}	5.90×10^{-4}	1.09×10^{-3}
		MFS	5.68×10^{-2}	3.51×10^{-2}	1.05×10^{-1}	1.23×10^{-1}	3.00×10^{-1}	3.34×10^{-1}	1.58×10^{0}
		HOS	1.00×10^{0}	1.77×10^{-3}	6.40×10^{-8}	4.63×10^{-8}	9.66×10^{-8}	7.96×10^{-7}	1.39×10^{-5}
	$\varepsilon = 0.2$	SFS	6.53×10^{-2}	3.62×10^{-3}	1.08×10^{-3}	1.10×10^{-3}	9.24×10^{-4}	3.03×10^{-3}	3.64×10^{-3}
		MFS	6.53×10^{-2}	3.46×10^{-2}	1.04×10^{-1}	1.33×10^{-1}	2.55×10^{-1}	3.11×10^{-1}	1.51×10^{0}
		HOS	1.00×10^{0}	7.07×10^{-2}	2.60×10^{-3}	2.86×10^{-3}	2.71×10^{-3}	2.53×10^{-3}	2.96×10^{-3}
	$\varepsilon = 0.4$	SFS	7.92×10^{-2}	3.99×10^{-3}	7.25×10^{-3}	8.44×10^{-3}	5.84×10^{-3}	2.38×10^{-2}	2.67×10^{-2}
		MFS	7.93×10^{-2}	3.59×10^{-2}	1.03×10^{-1}	1.43×10^{-1}	2.15×10^{-1}	2.91×10^{-1}	1.45×10^{0}
		HOS	1.00×10^{0}	1.42×10^{-1}	2.06×10^{-3}	2.24×10^{-2}	2.07×10^{-2}	1.92×10^{-2}	2.15×10^{-2}
Ω_2	$\varepsilon = 0.005$	SFS	4.67×10^{-2}	4.34×10^{-4}	2.31×10^{-4}	2.12×10^{-4}	2.62×10^{-4}	6.10×10^{-4}	1.28×10^{-3}
		MFS	4.67×10^{-2}	2.13×10^{-3}	7.51×10^{-3}	2.48×10^{-3}	1.70×10^{-2}	1.12×10^{-2}	4.42×10^{-1}
		HOS	1.00×10^{0}	2.50×10^{-3}	8.22×10^{-8}	4.40×10^{-8}	8.17×10^{-8}	6.63×10^{-7}	1.34×10^{-5}
	$\varepsilon = 0.2$	SFS	5.89×10^{-2}	4.77×10^{-4}	2.61×10^{-4}	1.88×10^{-4}	4.49×10^{-4}	1.59×10^{-3}	1.71×10^{-3}
		MFS	5.88×10^{-2}	1.26×10^{-3}	7.31×10^{-3}	3.25×10^{-3}	9.62×10^{-3}	1.05×10^{-2}	3.62×10^{-1}
		HOS	1.00×10^{0}	9.96×10^{-2}	2.68×10^{-3}	2.83×10^{-3}	2.54×10^{-3}	2.91×10^{-3}	1.78×10^{-3}
	$\varepsilon = 0.4$	SFS	7.39×10^{-2}	6.44×10^{-4}	4.95×10^{-4}	7.60×10^{-4}	4.03×10^{-3}	1.56×10^{-2}	5.31×10^{-3}
		MFS	7.37×10^{-2}	7.49×10^{-4}	6.98×10^{-3}	4.01×10^{-3}	5.74×10^{-3}	2.57×10^{-2}	2.92×10^{-1}
		HOS	1.00×10^{0}	1.97×10^{-1}	2.15×10^{-2}	2.23×10^{-2}	1.87×10^{-2}	2.13×10^{-2}	1.28×10^{-2}

waves. By contrast, the MFS method allows sources to be placed above the nonlinear free surface and supports flexible local refinement, which can significantly enhance accuracy. Consequently, for short-wavelength and strongly nonlinear waves, MFS can outperform the HOS method, particularly within region Ω_2.

Nevertheless, due to its high computational cost, MFS is restricted to solving the free-surface Dirichlet problem within a truncated domain of only $36\,\mathrm{m}\times36\,\mathrm{m}$. Since no boundary conditions are imposed outside this domain, information from the exterior region is missing, and the velocity potential induced outside the fundamental solution domain by the resulting source-strength distribution does not satisfy Eq. (16). As a result, the error of MFS increases rapidly with wavelength, especially near the edges of the fundamental solution domain.

The SFS method integrates the advantages of both HOS and MFS. On the one hand, it retains the large computational domain of HOS, covering $1024\,\mathrm{m}\times1024\,\mathrm{m}$; on the other hand, it allows local refinement in regions of interest (such as Ω_2) in a manner similar to MFS. This hybrid strategy enables SFS, with a computational cost comparable to that of MFS, to avoid truncation effects when simulating long waves and to achieve an accuracy close to that of HOS. Meanwhile, for short and strongly nonlinear waves, local refinement can be applied arbitrarily, yielding accuracy comparable to or even higher than that of MFS, and significantly better than that of HOS.

To further clarify the error characteristics of the different methods, the Dirichlet problem for the velocity potential is solved within the computational domain defined in this section with $\varepsilon = 0.2$ and $\lambda = 18\,\mathrm{m}$ using varying nodal spacings. Figure 7 presents the results. While the errors for all three methods eventually stabilize at high resolutions, SFS achieves the lowest error level once the mesh is sufficiently refined.

Figure 8 illustrates the spatial distribution of intrinsic errors at the highest resolution.

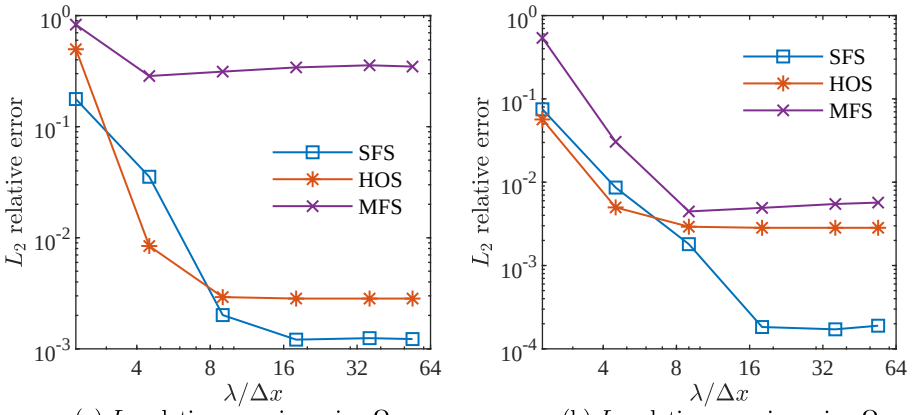

(a) L_2 relative error in region Ω_1 (b) L_2 relative error in region Ω_2

FIG. 7. Error variation with grid resolution for different methods ($\varepsilon = 0.2,\ \lambda = 18\,\mathrm{m}$)

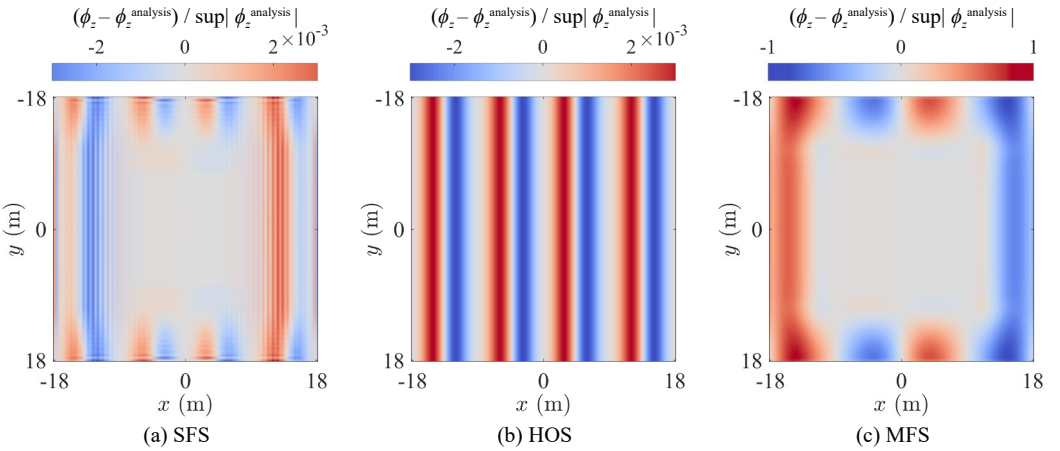

(a) SFS (b) HOS (c) MFS

FIG. 8. Spatial distribution of errors for different methods ($\varepsilon = 0.2,\ \lambda = 18\,\mathrm{m},\ \Delta x = 1/3\,\mathrm{m}$)

As shown in Fig. 8(b), the HOS solution exhibits a periodic error pattern with $\lambda/2$. This behavior arises from inaccuracies in the high-order modes when solving the perturbation expansion. For MFS, Fig. 8(c) shows that the error is concentrated near the edges of the computational domain and gradually decreases toward the interior region. The SFS solution exhibits characteristics of both methods. Its overall error magnitude distribution resembles that of MFS, with larger errors near the domain edges, while the edge pattern follows the HOS-type $\lambda/2$ periodic variation. This indicates that the SFS error is governed by both HOS modal inaccuracies and MFS edge effects, implying that improving its accuracy requires refinement of both components.

2. Dirichlet–Neumann problem: partially submerged hemisphere

This section further examines cases where flow disturbance is caused by a surface-piercing body. The computational setup follows Section III D 1, with a 1024 m × 1024 m spectral layer and a centrally located 36 m × 36 m fundamental solution region. At the center of the domain, a hemisphere with an 8 m diameter is placed, with grid refinement near the waterline, as shown in Fig. 9.

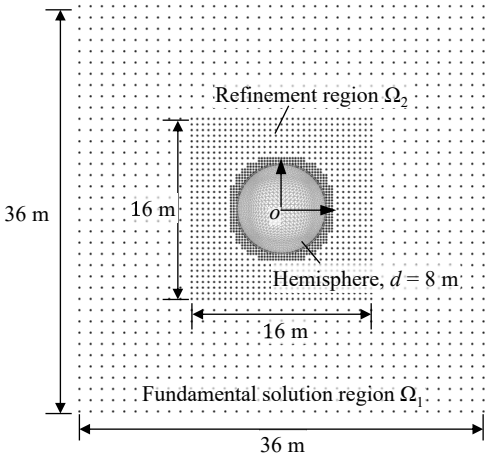

FIG. 9. Fundamental solution region containing a hemisphere.

The target velocity potential is defined as

$$\phi(x, y, z) = J_0(k\sqrt{x^2 + y^2})e^{kz} \tag{18}$$

where J_0 is the zeroth-order Bessel function. For simplicity, the free-surface boundary is set at $z = 0$. Dirichlet boundary conditions are imposed on the free surface, while Neumann conditions are applied to the hemisphere, both corresponding to Eq. (18).

Both the SFS and MFS methods are used to solve these boundary conditions. Since HOS cannot handle problems involving immersed bodies, it is excluded from this comparison. The resulting vertical velocity on the free surface is compared against the theoretical solution, as summarized in Table II. For short wavelengths, SFS and MFS yield similar error levels. As the wavelength increases, SFS exhibits improved accuracy over MFS. This difference arises because MFS limits boundary condition solutions to the truncated fundamental solution domain, which is insufficient to capture the full velocity potential, leading to higher numerical errors.

Figure 10 clearly illustrates the individual contributions of each SFS method component to the flow field. The method first determines $\boldsymbol{\sigma}_{\mathrm{f1}}$, which approximates the near-field Dirichlet condition as specified in Eq. (13a). It then efficiently computes the pseudo-spectral modal amplitudes $\boldsymbol{s}$, satisfying the far-field Dirichlet boundary and representing the major portion of the flow. Finally, $\boldsymbol{\sigma}_{\mathrm{f2}}$ and $\boldsymbol{\sigma}_{\mathrm{b}}$ are solved. Figure 10 shows that the velocity potential induced by $\boldsymbol{\sigma}_{\mathrm{f2}}$ and $\boldsymbol{\sigma}_{\mathrm{b}}$ vanishes on the free surface and has only a minor effect on the flow near the structure.

TABLE II. Comparison of L_2 relative errors in simulating Bessel harmonic functions with various wave lengths using different methods.

		λ (m)						
		2	4	8	16	32	64	128
Ω_1	SFS	3.39×10^{-2}	1.48×10^{-2}	1.15×10^{-2}	6.75×10^{-3}	2.76×10^{-3}	1.40×10^{-3}	1.29×10^{-3}
	MFS	1.06×10^{-1}	5.85×10^{-2}	5.36×10^{-2}	1.06×10^{-1}	9.12×10^{-2}	3.06×10^{-1}	1.38×10^{-1}
Ω_2	SFS	3.31×10^{-2}	1.65×10^{-2}	1.25×10^{-2}	7.78×10^{-3}	2.85×10^{-3}	1.44×10^{-3}	1.22×10^{-3}
	MFS	2.68×10^{-2}	1.27×10^{-2}	1.33×10^{-2}	3.39×10^{-2}	4.99×10^{-2}	1.62×10^{-1}	1.44×10^{-1}

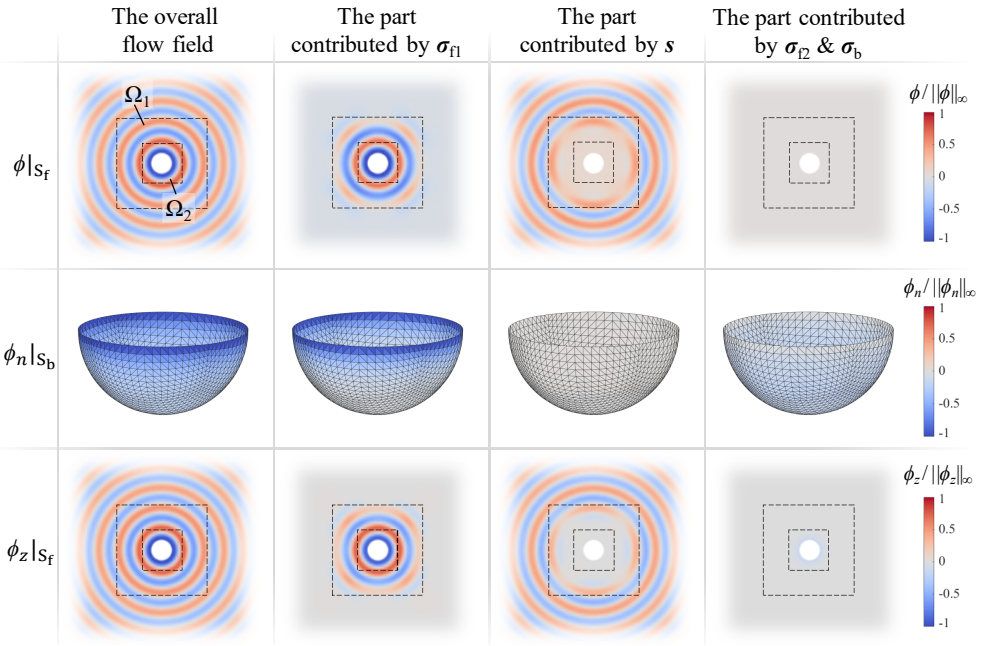

FIG. 10. Contributions of each component to the overall flow field in the SFS method ($\lambda = 8\,\mathrm{m}$). The dashed square region on the free surface indicates where the fundamental solutions are arranged.

All computations in this study were carried out on a computer equipped with an AMD Ryzen 7 9700X CPU and an AMD Radeon RX 9070 GRE GPU. An in-house potential flow solver with GPU acceleration was employed (details regarding GPU implementation are available in [38]). Table III summarizes the computation times for each step in calculating ϕ_z using the SFS method, comparing results with and without GPU acceleration. Each value represents the average of 1000 runs.

As shown in Table III, the additional computational cost of the SFS method compared to MFS mainly arises from the construction of the boundary condition in Eq. (13b), that is, from accounting for the influence of $\boldsymbol{\sigma}_{f1}$ on the free-surface boundary. Even when accelerated by the Barnes-Hut algorithm, calculating the velocity potential induced by $\boldsymbol{\sigma}_{f1}$ over 1024×1024 spectral collocation points remains computationally intensive. Furthermore, although the matrix structures for solving $\boldsymbol{\sigma}_{f2}$ and $\boldsymbol{\sigma}_b$ are the same in both SFS and MFS methods,

the computation times differ. This is due to the use of the GMRES iterative solver; when applying SFS, the Dirichlet condition on the free surface is set to zero, which typically allows the solver to converge in fewer iterations than in the MFS approach.

The comparison of computation times demonstrates that SFS successfully expands the nonlinear computational domain from $36\,\mathrm{m} \times 36\,\mathrm{m}$ in MFS to $1024\,\mathrm{m} \times 1024\,\mathrm{m}$, with a manageable computational cost. This 800-fold increase in domain size significantly improves the simulation's ability to capture larger-scale flow features and greatly reduces errors associated with domain truncation.

TABLE III. Computational time for each step of the SFS method

	SFS		MFS	
	W/o GPU acc.	W/ GPU acc.	W/o GPU acc.	W/ GPU acc.
Solve $\boldsymbol{\sigma}_{\mathrm{f1}}$ in Eq. (13a)	169.2 ms	53.6 ms	/	/
Construct B.C. in Eq. (13b)	431.3 ms	199.2 ms	/	/
Solve $\boldsymbol{s}$ in Eq. (13b)	29.5 ms	5.8 ms	/	/
Construct B.C. in Eq. (13c)	51.7 ms	35.9 ms	/	/
Solve $\boldsymbol{\sigma}_{\mathrm{f2}}$ and $\boldsymbol{\sigma}_{\mathrm{b}}$	798.2 ms	147.8 ms	1128.7 ms	225.6 ms
Total	1479.9 ms	442.3 ms	1128.7 ms	225.6 ms

IV. LARGE-SCALE SHIP WAKE SIMULATION

A. Numerical setup

In this section, numerical results are presented for a Series 60 (S60) ship model with a block coefficient $C_{\mathrm{B}} = 0.6$ and a length $L = 3\,\mathrm{m}$. The SFS simulation yields a background spectral layer with 4096×4096 grids and a grid spacing of $0.12\,\mathrm{m}$, resulting in a nonlinear computational domain that exceeds $160L$ in size. The ship hull panels and free-surface nodes within the fundamental solution domain are shown in Fig. 11, where the transition width of the weight function l_w is set to $1.44\,\mathrm{m}$. At a Froude number $Fn = U/\sqrt{gL} = 0.316$, the steady-state simulation includes 2,566 ship hull panels and 5,343 free-surface source points. Each simulation comprises 8,000 time steps, with each case requiring approximately 3.2 CPU hours of computation.

During the simulation, the ship initially accelerates from rest along the x-axis at $0.1g$, then transitions to constant-speed straight-line motion upon reaching the target velocity. Multiple earth-fixed wave probes (P1, P2, and P3) are placed $40L_{\mathrm{pp}}$ ahead of the ship's initial position, as shown in Fig. 12. The probes are aligned in the y-direction, and located at transverse distances of $0.5L$, $3.0L$, and $8.0L$ from the ship, respectively.

B. Nonlinear ship wake patterns

To validate the proposed methodology, we first compare near-field nonlinear ship wakes simulated by the SFS method with both experimental data and previous numerical results. Figure 13 shows the simulated wake patterns alongside experimental measurements from

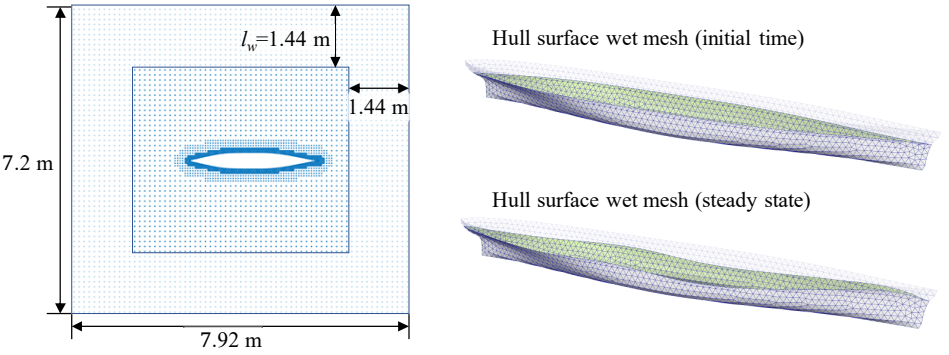

(a) Node arrangement in the fundamental solution region

(b) Mesh distribution on the hull surface (color indicates normal direction; translucent panels excluded from calculation)

FIG. 11. Node distribution of the free surface and hull surface mesh for the Series 60 (S60) model simulation.

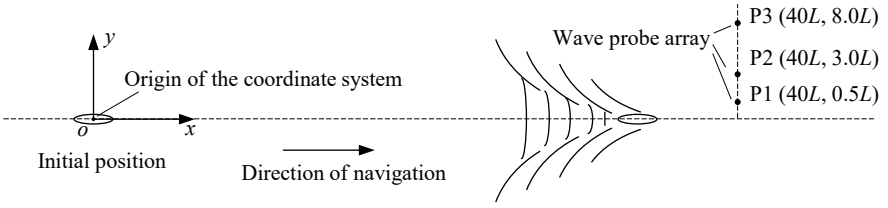

FIG. 12. Probe layout for numerical simulation of ship wake.

Toda *et al.* [43]. The results demonstrate that the SFS simulation closely matches experimental observations, accurately capturing the positions of wave crests and troughs.

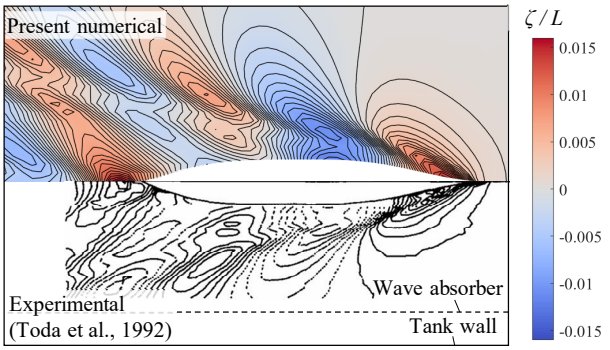

FIG. 13. Comparison of wave patterns for the S60 ship simulated by the present method and experimental measurements.

Further comparisons of hull-side wave profiles at various Froude numbers are presented in Fig. 14. The experimental data are drawn from Takeshi and Hino [44], while results labeled "linear" correspond to simulations using the linear Rankine source method from Tarafder and Suzuki [45]. The nonlinear SFS method accurately reproduces the hull-side wave profiles and shows excellent agreement with the experimental measurements, outperforming the linear method, demonstrating the effectiveness of the SFS approach for modeling nonlinear ship wakes.

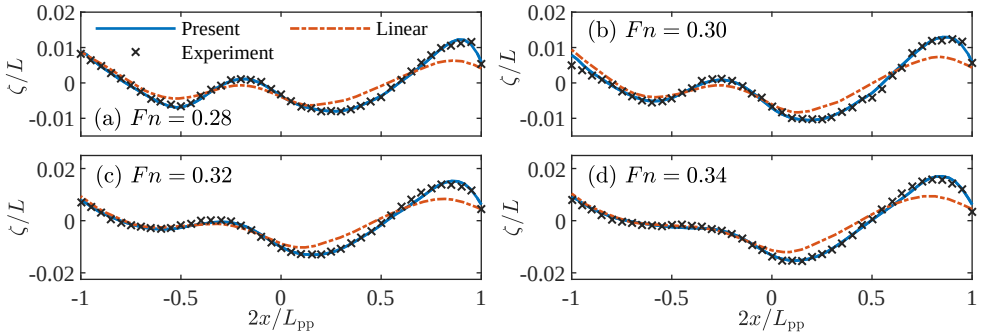

FIG. 14. Comparison of hull-side wave profiles of the S60 hull by different methods.

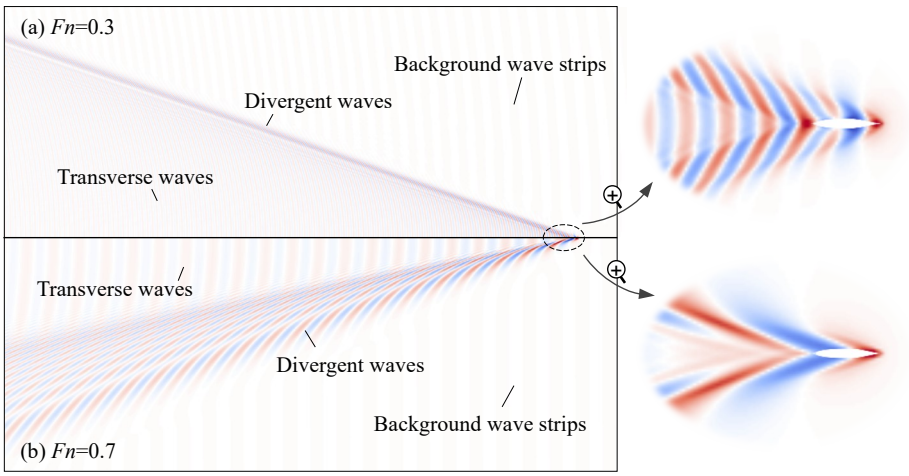

FIG. 15. Large-scale wave patterns of S60 ship wake at different Froude numbers. (a) $Fn = 0.3$, and (b) $Fn = 0.7$.

Figure 15 presents large-scale nonlinear wake patterns at Froude numbers $Fn = 0.3$ and $Fn = 0.7$. Both transverse and divergent wave systems are clearly observed. At $Fn = 0.3$, the characteristic wavelength is shorter and the wake is dominated by transverse waves. In contrast, at $Fn = 0.7$, the wavelength increases and the divergent component becomes predominant. Faint background wave bands are also visible; the origin and features of these patterns will be discussed in the following sections.

C. Spectrogram analysis

The upper panels of Figs. 16 and 17 present the time histories of wave heights recorded at various probes. Applying a short-time Fourier transform (STFT) to these records yields the spectrograms shown in the lower panels. In these spectrograms, the horizontal axis is non-dimensionalized as $t' = Ut/L$. The vertical axis, $\omega' = U\omega/g$, gives the wave frequency normalized by the characteristic frequency of the ship wake. Color intensity indicates the power density of each frequency component over time. These visualizations reveal multiple distinct wave components, providing new insights into the spatial distribution and generation mechanisms of nonlinear ship wakes.

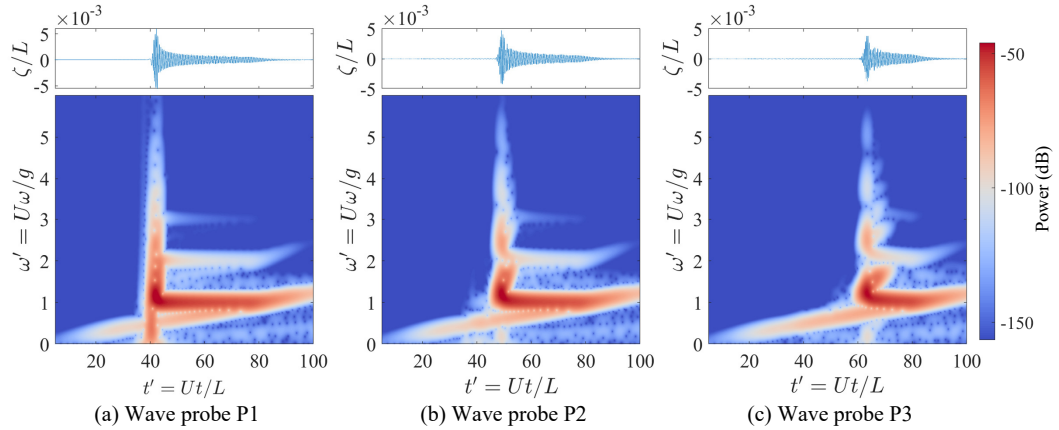

FIG. 16. Spectrograms of nonlinear ship waves at $Fn = 0.3$. (a) Wave probe P1, (b) Wave probe P2, and (c) Wave probe P3.

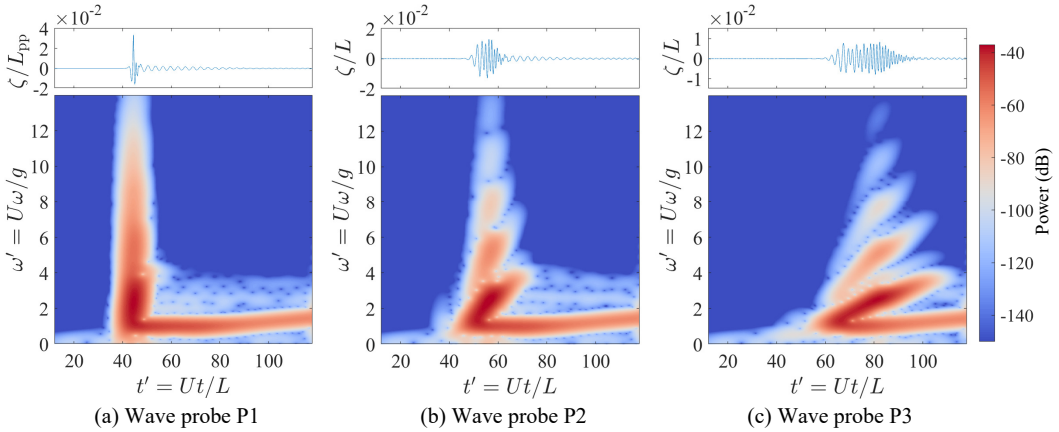

FIG. 17. Spectrograms of nonlinear ship waves at $Fn = 0.7$. (a) Wave probe P1, (b) Wave probe P2, and (c) Wave probe P3.

1. Linear wave components

Within the framework of linear theory, the spectrogram of a steadily moving ship's wake is expected to contain two distinct wave components. Below, we briefly outline the derivation; similar derivations are also presented in Torsvik *et al.* [18] and Pethiyagoda *et al.* [36].

As illustrated in Fig. 18, when a wave reaches the probe, it may have originated when the ship previously passed point O; at this moment, the ship is located at point M. According to stationary phase theory, a disturbance moving steadily generates waves that propagate at different speeds and in different directions. The relationship between the phase velocity c_{phase} and the propagation angle θ is given by

$$c_{\text{phase}}(\theta) = U\cos\theta, \tag{19}$$

Since the group velocity is half the phase velocity, when the ship reaches point M, the waves generated at point O will have arrived precisely at the circle indicated by the dashed line in Fig. 18. Let x denote the longitudinal distance from the probe to the ship, and y the transverse distance. The resulting geometry leads to the following relationship:

$$x - y\tan\theta = \frac{y}{\tan\theta} + y\tan\theta. \tag{20}$$

Solving Eq. (20) gives the propagation angles for the two linear wave components:

$$\tan\theta_{1,2} = \frac{(x/y) \mp \sqrt{(x/y)^2 - 8}}{4}, \tag{21}$$

For linear waves, the dispersion relation $c_{\text{phase}} = g/\omega$ applies, so the corresponding wave frequency for a given angle θ can be expressed as

$$\omega'(\theta) = \frac{U\omega(\theta)}{g} = \frac{U}{c_{\text{phase}}(\theta)} = \frac{1}{\cos\theta}. \tag{22}$$

and the non-dimensional frequencies for the two linear wave components are

$$\omega'_{1,2} = \frac{1}{\cos\theta_{1,2}} = \frac{\sqrt{2}}{4}\sqrt{(x/y)^2 \mp (x/y)\sqrt{(x/y)^2 - 8} + 4}. \tag{23}$$

At each time t', the values of x and y can be determined by the ship's position and substituted into Eq. (23) to obtain $\omega'_{1,2}$.

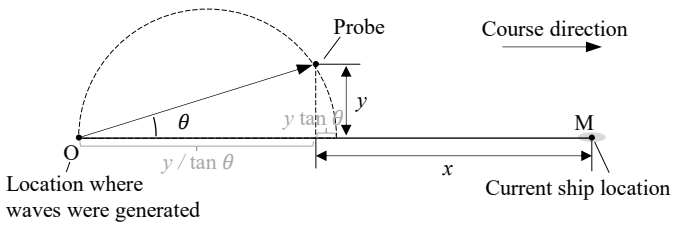

FIG. 18. Schematic diagram of the wave component detected at a given moment.

In Fig. 19, the solid lines indicate the time–frequency tracks predicted by linear theory, corresponding well with regions of highest energy density and representing the main wake components. As the distance between the probe and the ship increases, the frequency along the ω_1' curve approaches 1, reflecting the classical transverse wave component. In contrast, the ω_2' curve shifts to higher frequencies with distance, representing the divergent wave component.

Figure 20 shows that at $Fn = 0.3$, the transverse wave system (ω_1') dominates, whereas the energy of the divergent waves (ω_2') diminishes rapidly over distance and time. Comparing spectrograms from different probe locations reveals that the temporal and spatial concentration of divergent wave energy depends strongly on the transverse distance from the ship track: more distant probes (e.g., Probe P3) detect divergent energy over a longer time window, illustrated by $t' \in [60, 70]$, while probes closer to the track (e.g., Probe P1) register noticeable divergent waves only near $t' = 40$.

Further results for $Fn = 0.7$ are shown in Fig. 21. At higher speeds, the divergent component is much more pronounced and constitutes a larger share of the total energy, making it easier to observe. For example, at Probe P3, the divergent wave energy persists over $t' \in [60, 100]$ and $\omega' \in [1, 4]$.

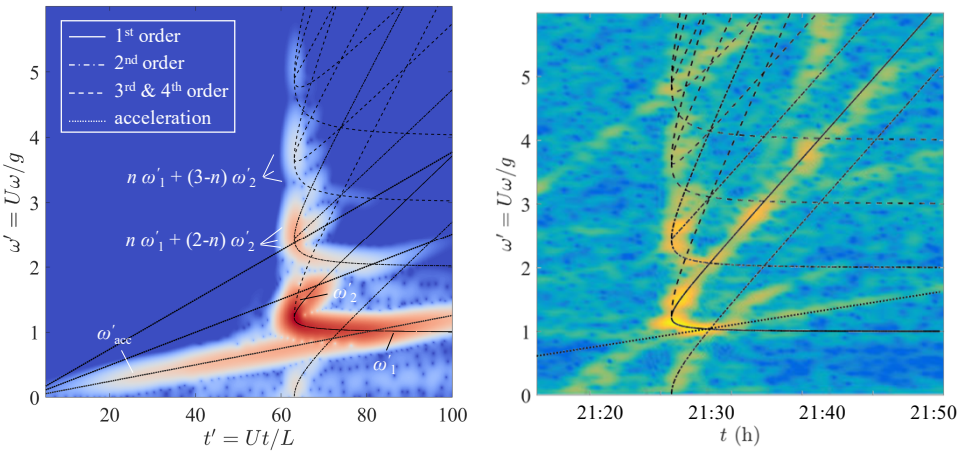

(a) Numerically simulated spectrogram

(b) Real-world measured spectrogram

FIG. 19. Various wave-making components in the spectrogram. (a) Spectrogram of the S60 model at $Fn = 0.3$ from numerical simulations. (b) Spectrogram of a high-speed ferry measured in the Gulf of Finland, plotted by Pethiyagoda *et al.* [36] based on data from Didenkulova *et al.* [46].

2. *Nonlinear wave components*

Beyond the two primary linear frequency bands, the spectrograms reveal several additional energy bands associated with nonlinear wave components. Perturbation theory explains these features by showing that higher-order components are generated through interactions among lower-order wave components, with their frequencies arising as sums and differences of the first-order frequencies. Figure 19 illustrates and categorizes these various

wave components. The positions of these nonlinear bands within the spectrogram align well with theoretical predictions, appearing as combinations of the primary linear bands.

Figure 19(a) displays the spectrogram for large-scale nonlinear ship wakes simulated using the SFS method, while Fig. 19(b) shows experimental results based on wave records from the Gulf of Finland [46]. Despite differences in ship type and speed, both spectrograms exhibit similar patterns, with multiple higher-order components clearly visible. Their locations closely follow the curves forecasted by perturbation theory, indicating that nonlinear energy transfer predominantly takes place through processes such as frequency doubling, summing, and differencing, which collectively confine wave energy to specific bands.

Previous research by Pethiyagoda *et al.* [36] first reported second-order components in the spectrograms of wakes generated by moving pressure sources. In contrast, the SFS method applied here successfully simulates nonlinear wakes from displacement ships, characterized by deeper drafts and stronger nonlinear effects. As shown in Fig. 19, the numerical results clearly demonstrate third- and fourth-order nonlinear components, providing additional support for earlier findings. Examining energy distribution, the amplitudes of first-, second-, and third-order components decrease by roughly an order of magnitude with each successive order. The agreement between the numerical and experimental spectrograms further clarifies the origins of high-frequency components observed in practice.

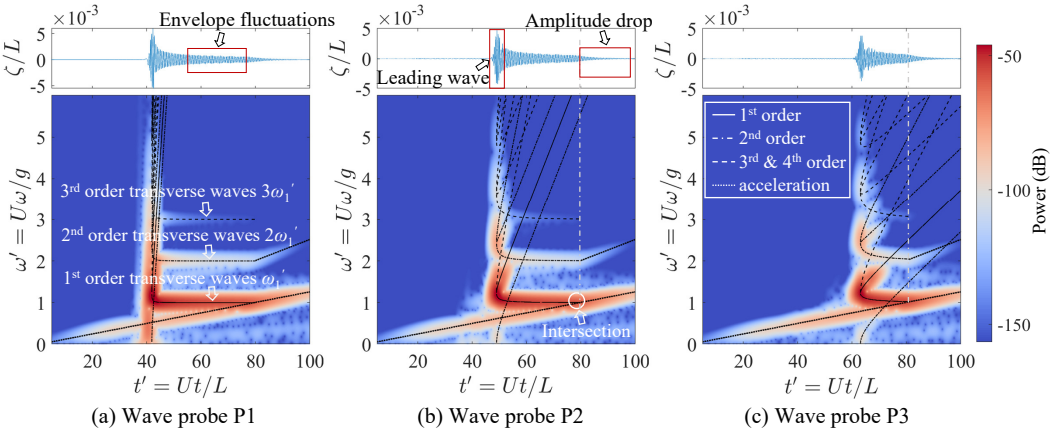

FIG. 20. Comparison of the spectrogram from numerical simulations with theoretical prediction curves ($Fn = 0.3$). (a) Wave probe P1, (b) Wave probe P2, and (c) Wave probe P3.

Figures 20 and 21 compare the simulated spectrograms with the theoretical prediction curves. The figures show that most of the high-frequency energy in the wake spectrogram arises from higher-order wave components. Within these, the higher-order divergent wave systems are particularly dominant. At $Fn = 0.3$, the first-order transverse wave system is energetically dominant, but the energy of higher-order transverse waves decays rapidly, with third-order transverse waves being nearly imperceptible in the spectrograms. In contrast, higher-order divergent wave systems remain apparent, with even fourth-order divergent components observable in the frequency spectrum. At $Fn = 0.7$, the divergent wave system is even more prominent throughout the time history, and in the spectrogram of Probe P2 (Fig. 21(b)), fifth-order nonlinear wake components can be clearly identified.

These findings suggest that the energy of nonlinear wake components does not simply scale

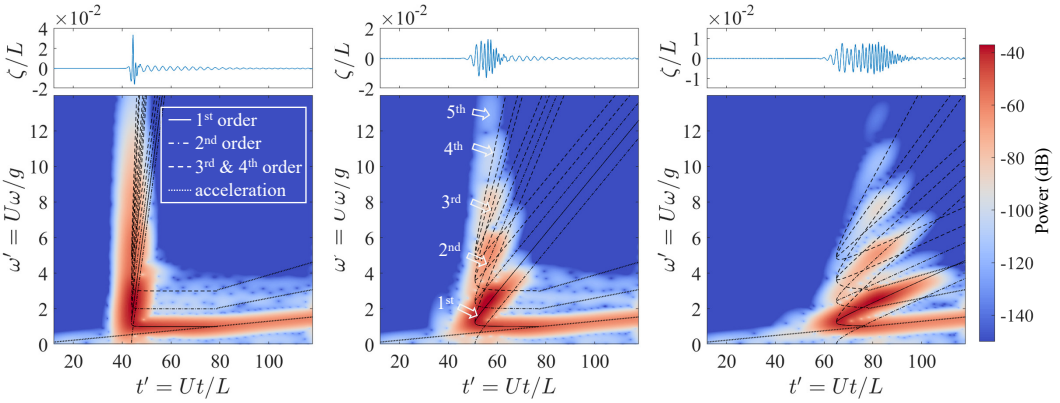

(a) Wave probe P1 (b) Wave probe P2 (c) Wave probe P3

FIG. 21. Comparison of the spectrogram from numerical simulations with theoretical prediction curves ($Fn = 0.7$). (a) Wave probe P1, (b) Wave probe P2, and (c) Wave probe P3.

with the product of first-order terms, but instead follows a distinct energy transfer mechanism. One possible explanation is that the divergent wave components, due to their higher frequencies and steeper wave slopes, experience more substantial nonlinear interactions.

3. Unsteady wave components

In addition to the steady linear and nonlinear wake components, the simulated spectrograms exhibit a distinct straight band spanning the entire time–frequency domain. In the spatial domain, this feature corresponds to the background stripes visible in Fig. 15. In the time series, this band overlaps with the transverse wave system, resulting in observable fluctuations in the wave envelope; for example, Fig. 20(a) shows fluctuations during $t' \in [60, 80]$. Such unsteady disturbances are frequently seen in towing tank experiments [47]. The spectrogram analysis presented here provides a new perspective on the origin of these phenomena.

A likely origin for these components is the unsteady wake generated during the ship's acceleration phase. Consider a disturbance occurring at time t_0 at position (x, y); if a wave generated by this disturbance is detected at time t, the group velocity c_{group} and phase velocity c_{phase} are related by

$$c_{\text{group}} = \frac{1}{2} c_{\text{phase}} = \frac{\sqrt{x^2 + y^2}}{t - t_0}. \tag{24}$$

According to the dispersion relation, the dimensionless frequency recorded at the probe is:

$$\omega' = \frac{U}{c_{\text{phase}}} = \frac{U(t - t_0)}{2\sqrt{x^2 + y^2}}. \tag{25}$$

In our simulations, the ship accelerates from rest at $a = 0.1g$ until reaching the target speed, then transitions to steady motion. The duration of acceleration is very short, allowing

this process to be approximated as an instantaneous disturbance. By substituting this simplified acceleration into Eq. (25), the theoretical curve ω'_{acc} is plotted in the spectrograms in Figs. 19–21. The observed energy band aligns closely with the theoretical time–frequency curve, supporting the interpretation that this band originates from acceleration-induced disturbances.

Figs. 20 and 21 show that the transverse wave band ω'_1 and the acceleration-induced band ω'_{acc} intersect at $t' \approx 80$. Beyond this point, the transverse component vanishes from the spectrogram. This is because the transverse wave travels at a constant speed: the later the wave reaches the probe, the farther the ship was from the probe at the time of generation. The transverse wave generated from the ship's initial position arrives at the probe around $t' \approx 80$, and before this, the ship was stationary and did not create a wave. Accordingly, the band does not appear in the spectrogram, and in the wave height time series, this is seen as a sudden drop in amplitude. This principle enables inference of the ship's starting position from the wave height history at a given measurement point.

Additionally, Figs. 20(a) and (b) show that the second-order transverse wave band is also truncated after $t' \approx 80$. This indicates that higher-order transverse waves propagate at the same speed as the first-order component, rather than following the linear dispersion relation. In contrast, in Fig. 21(c), the band corresponding to the divergent wave component ω'_2, which has a higher frequency and lower speed, does not intersect with the acceleration band, so divergent components persist after $t' \approx 80$.

D. Leading wave and wake angle

As shown in Fig. 20, a prominent peak in wave amplitude typically appears in the time series shortly after the wake reaches the measurement point. In the spectrogram, this corresponds to a vertical energy band spanning nearly the entire frequency range, which Torsvik *et al.* [18] termed the *leading wave*. Our nonlinear simulations clearly indicate that this vertical energy band results from the superposition of linear and nonlinear wake components of various orders. At measurement positions close to the ship (such as wave probe P1), the slope of the divergent wave's time–frequency curve is steeper, causing energy to concentrate within a shorter time window and forming a larger leading wave peak. Conversely, at more distant locations (e.g., wave probe P3), these wave components are more evenly distributed over time, resulting in a smaller leading wave.

The scenario in Fig. 21 presents a difference. At higher speeds, the divergent wave system accounts for a greater share of the wake energy. At wave probe P1, the spectrogram reveals a pronounced vertical energy band, and the leading wave appears as a sharper, more abrupt peak in the time series. In contrast, at P2 and P3, higher-order divergent waves dominate, with their energy persisting considerably longer than in the $Fn = 0.3$ case and spreading more gradually over time. As a result, the time series at P2 and P3 show no distinct leading wave, but instead sustained oscillations of similar amplitude with gradually decreasing periods.

This analysis of the leading wave helps explain the visually observed wake angle for high-speed ships. Satellite and synthetic aperture radar (SAR) images show that the apparent wake angle of fast vessels is narrower than the $19°28'$ predicted by Kelvin's theory. This phenomenon, first reported by Rabaud and Moisy [48], has attracted considerable interest. Figure 22 displays simulated three-dimensional wave patterns of the S60 hull at two Froude numbers. For $Fn = 0.3$, the wake is confined within the classical Kelvin angle, in line

with theoretical predictions, whereas for $Fn = 0.7$, the observed wake angle is noticeably narrower.

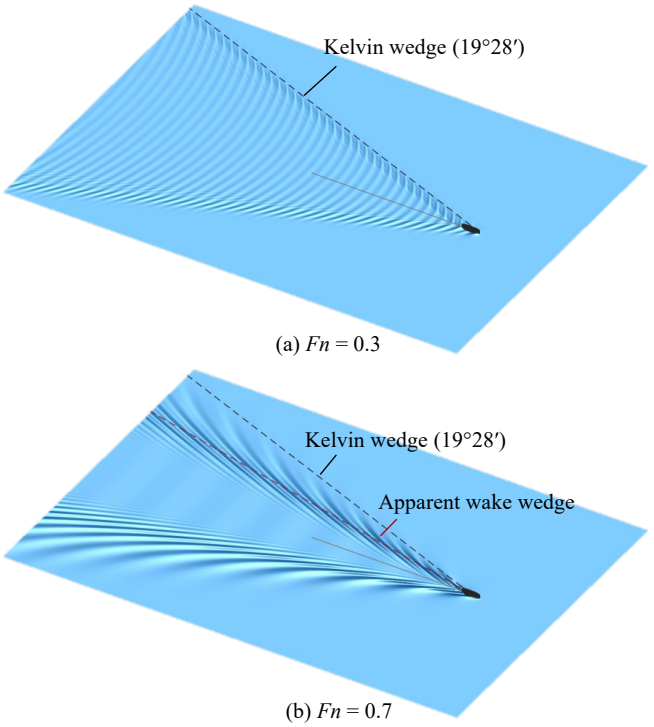

FIG. 22. Three-dimensional wave patterns and wake angles of the S60 hull at different Froude numbers. (a) $Fn = 0.3$, (b) $Fn = 0.7$.

Darmon *et al.* [16] pointed out that for high-speed ships, the apparent wake angle is not determined by the cusps of a Kelvin wave pattern. Instead, observers tend to regard the lines formed by wake crests as the wake system. At $Fn = 0.3$, the leading wave crest closely aligns with the Kelvin cusp locations, yielding a wake angle that matches Kelvin's prediction. In contrast, at $Fn = 0.7$, the leading wave is absent in the far field, and multiple divergent wave components of comparable amplitude are distributed within a spatial region. As shown in Fig. 21(c), wake crests maintain similar amplitudes over $t' \in [66, 85]$, with the maximum peak near $t' = 82$, rather than at the initial arrival time $t' = 66$. Additionally, as seen in Fig. 22, the inner divergent waves within the wake angle develop shorter wavelengths and greater steepness compared to those outside, likely resulting in more pronounced visual shading and reflection due to light. Collectively, these findings suggest that the perceived boundary of a high-speed ship's wake is shaped by a combination of wave steepness, height, and light effects. The absence of a clear leading wave, along with increased steepness of inner divergent waves, contributes to the visual impression of a narrower wake angle at higher speeds.

V. CONCLUSION

In this work, we have proposed an SFS method that enables efficient simulation of nonlinear wave–structure interactions in ocean environments. The approach regards the flow field as a superposition of spectral basis functions and fundamental solutions. Fundamental solutions are distributed in the near-field, allowing for detailed resolution of local flow phenomena, while spectral basis functions characterize the far-field flow. By leveraging the linearity of the Laplace equation, the original boundary value problem is elegantly decomposed into multiple subproblems, facilitating separate computation of spectral coefficients and fundamental source strengths. Numerical validation, both for domains with and without bodies, demonstrates that the SFS method integrates the advantages of HOS and MFS. The method efficiently simulates large-scale nonlinear free surfaces with $O(N \log N)$ complexity and allows for near-field placement of fundamental solutions to capture the effects of surface-piercing boundaries. Compared to traditional HOS methods, SFS enables using a greater number of near-field unknowns, yielding finer resolution of flow features and improved accuracy for short wavelengths and steep waves. Relative to MFS, SFS utilizes the spectral layer to greatly expand the nonlinear computational domain, achieving domain sizes tens to hundreds of times larger at similar computational cost, resulting in enhanced accuracy for long-wave simulations.

To demonstrate and validate the method, we simulated fully nonlinear ship wakes for a Series 60 hull in an ultra-large domain of $160L_{\mathrm{pp}} \times 160L_{\mathrm{pp}}$. To our knowledge, this is the first numerical study of nonlinear wakes for displacement vessels at such scale. The simulated wake patterns show good agreement with experimental measurements, confirming the reliability of the approach. Analysis of the results reveals distinct higher-order nonlinear wave components in the time–frequency spectrogram, shedding light on the origins of various wake features observed in the experiments of Didenkulova *et al.* [46]. Higher-order nonlinear components in the spectrogram appear as sums of first-order components, with divergent waves exhibiting more pronounced nonlinear characteristics than transverse waves. Additionally, our simulations reveal wake features associated with vessel acceleration, which present as straight bands in the spectrogram. Finally, we discuss the spatial and frequency distribution of the leading wave, offering new insight into reduced wake angles for high-speed ships.

The SFS method proposed here is not limited to steady straight-line navigation; it is also well-suited for a wide range of unsteady ocean engineering problems, including interactions among incident waves and multiple floating bodies. Nevertheless, due to the constraints of potential flow theory, SFS cannot model viscous effects or wave breaking. In future work, we aim to extend this framework to the Navier–Stokes equations, combining spectral methods for the inviscid outer flow with finite volume approaches in the viscous near field, eventually achieving two-way coupling of viscous and potential flows.

ACKNOWLEDGMENTS

This work was supported by the Hainan Natural Science Foundation Youth Fund (Grant No. 525QN399) and the Natural Science Foundation of Shanghai (Grant No. 25ZR1402240), which the authors gratefully acknowledge.

The authors acknowledge the limited use of ChatGPT-4.0 as an auxiliary tool for the initial translation of selected portions of this manuscript. All AI-assisted content was sub-

sequently reviewed, edited, and rephrased by the authors, for which full responsibility is taken by the authors.

DATA AVAILABILITY

The data that support the findings of this article are openly available at [49].

[1] J. Rapaglia, L. Zaggia, K. Parnell, G. Lorenzetti, and A. T. Vafeidis, Ship-wake induced sediment remobilization: Effects and proposed management strategies for the Venice Lagoon, Ocean Coast. Manage. **110**, 1 (2015).

[2] S. D. Meyers, M. E. Luther, S. Ringuet, G. Raulerson, E. Sherwood, K. Conrad, and G. Basili, Ship wakes and their potential shoreline impact in Tampa Bay, Ocean Coast. Manage. **211**, 105749 (2021).

[3] A. C. Muscalus and K. A. Haas, Vessel wake contributions to erosion at exposed and sheltered shorelines near a tidal shipping channel, Coast. Eng. **178**, 104220 (2022).

[4] T. Soomere, Nonlinear components of ship wake waves, Appl. Mech. Rev. **60**, 120 (2007).

[5] C. Forlini, R. Qayyum, M. Malej, M.-A. Y.-H. Lam, F. Shi, C. Angelini, and A. Sheremet, On the problem of modeling the boat wake climate: The Florida intracoastal waterway, J. Geophys. Res. Oceans **126**, e2020JC016676 (2021).

[6] L. Zhou, H. S. Abdelwahab, and C. G. Soares, Experimental and CFD investigation of the effects of a high-speed passing ship on a moored container ship, Ocean Eng. **228**, 108914 (2021).

[7] R. Sreedevi and S. Nallayarasu, Investigation on ship mooring forces including passing ship effects validated by experiments, Ocean Eng. **283**, 115004 (2023).

[8] W. Thomson, On ship waves, Proc. Inst. Mech. Engrs. **38**, 409 (1887).

[9] J. H. Michell, The wave-resistance of a ship, Lond. Edinb. Phil. Mag **45**, 106 (1898).

[10] E. O. Tuck, D. C. Scullen, and L. Lazauskas, Ship-wave patterns in the spirit of Michell, in *IUTAM Symposium on Free Surface Flows: Proceedings of the IUTAM Symposium* (Springer, Birmingham, United Kingdom, 2001) pp. 311–318.

[11] T. H. Havelock, The theory of wave resistance, Proc. R. Soc. London A. **138**, 339 (1932).

[12] D. C. Scullen and E. O. Tuck, Free-surface elevation due to moving pressure distributions in three dimensions, J. Eng. Math. **70**, 29 (2011).

[13] R. Brard, The representation of a given ship form by singularity distributions when the boundary condition on the free surface is linearized, J. Ship Res. **16**, 79 (1972).

[14] F. Noblesse, F. Huang, and C. Yang, The Neumann–Michell theory of ship waves, J. Eng. Math. **79**, 51 (2013).

[15] F. Noblesse, J. He, Y. Zhu, L. Hong, C. Zhang, R. Zhu, and C. Yang, Why can ship wakes appear narrower than Kelvin's angle?, Eur. J. Mech. B Fluids **46**, 164 (2014).

[16] A. Darmon, M. Benzaquen, and E. Raphaël, Kelvin wake pattern at large Froude numbers, J. Fluid Mech. **738**, R3 (2014).

[17] R. Pethiyagoda, T. J. Moroney, C. J. Lustri, and S. W. McCue, Kelvin wake pattern at small Froude numbers, J. Fluid Mech. **915**, A126 (2021).

[18] T. Torsvik, T. Soomere, I. Didenkulova, and A. Sheremet, Identification of ship wake structures by a time–frequency method, J. Fluid Mech. **765**, 229 (2015).

[19] R. Pethiyagoda, T. J. Moroney, G. J. Macfarlane, and S. W. McCue, Spectrogram analysis of surface elevation signals due to accelerating ships, Phys. Rev. Fluids **6**, 104803 (2021).

[20] H. Liang, Y. Li, and X. Chen, An Earth-fixed observer to ship waves, J. Fluid Mech. **984**, A14 (2024).

[21] Q. X. Wang, Unstructured MEL modelling of nonlinear unsteady ship waves, J. Comput. Phys. **210**, 368 (2005).
[22] F. Kara, C. Q. Tang, and D. Vassalos, Time domain three-dimensional fully nonlinear computations of steady body–wave interaction problem, Ocean Eng. **34**, 776 (2007).
[23] X. Chen, R. Zhu, C. Ma, and J. Fan, Computations of linear and nonlinear ship waves by higher-order boundary element method, Ocean Eng. **114**, 142 (2016).
[24] J. C. Harris, E. Dombre, M. Benoit, S. T. Grilli, and K. I. Kuznetsov, Nonlinear time-domain wave-structure interaction: A parallel fast integral equation approach, Int. J. Numer. Meth. Fl. **94**, 188 (2022).
[25] H. Yan and Y. Liu, An efficient high-order boundary element method for nonlinear wave–wave and wave-body interactions, J. Comput. Phys. **230**, 402 (2011).
[26] J. S. de Medeiros, Y. Liu, and D. K. P. Yue, A fast high-order boundary element method for nonlinear water waves generation and propagation in large wave basins, Comput. Method. Appl. M. **432**, 117396 (2024).
[27] A. P. Engsig-Karup, C. Eskilsson, and D. Bigoni, A stabilised nodal spectral element method for fully nonlinear water waves, J. Comput. Phys. **318**, 1 (2016).
[28] F. Robaux and M. Benoit, Development and validation of a numerical wave tank based on the harmonic polynomial cell and immersed boundary methods to model nonlinear wave-structure interaction, J. Comput. Phys. **446**, 110560 (2021).
[29] J. Visbech, A. P. Engsig-Karup, and H. B. Bingham, Solving the complete pseudo-impulsive radiation and diffraction problem using a spectral element method, Comput. Method. Appl. M. **423**, 116871 (2024).
[30] C. Tong, Y. Shao, H. B. Bingham, and F.-C. W. Hanssen, An adaptive harmonic polynomial cell method for three-dimensional fully nonlinear wave-structure interaction with immersed boundaries, Phys. Fluids **36** (2024).
[31] S. H. Rhee and F. Stern, Unsteady RANS method for surface ship boundary layer and wake and wave field, Int. J. Numer. Meth. Fl **37**, 445 (2001).
[32] Q. Zeng, R. Hekkenberg, C. Thill, and H. Hopman, Scale effects on the wave-making resistance of ships sailing in shallow water, Ocean Eng. **212**, 107654 (2020).
[33] Z. Zhang and K. Maki, Wave resistance of a ship moving in a lead between rigid ice sheets of finite thickness, Phys. Fluids **35** (2023).
[34] L. K. Forbes, An algorithm for 3-dimensional free-surface problems in hydrodynamics, J. Comput. Phys. **82**, 330 (1989).
[35] R. Pethiyagoda, S. W. McCue, T. J. Moroney, and J. M. Back, Jacobian-free Newton–Krylov methods with GPU acceleration for computing nonlinear ship wave patterns, J. Comput. Phys. **269**, 297 (2014).
[36] R. Pethiyagoda, S. W. McCue, and T. J. Moroney, Spectrograms of ship wakes: identifying linear and nonlinear wave signals, J. Fluid Mech. **811**, 189 (2017).
[37] See supplemental material at [url] for a simple demo program of the SFS method.
[38] K. Shi and R. Zhu, Efficient spectral coupled boundary element method for fully nonlinear wave–structure interaction simulation, Phys. Fluids **35** (2023).
[39] Y. Cao, W. W. Schultz, and R. F. Beck, Three-dimensional desingularized boundary integral methods for potential problems, Int. J. Numer. Meth. Fl **12**, 785 (1991).
[40] J. Barnes and P. Hut, A hierarchical O(NlogN) force-calculation algorithm, Nature **324**, 446 (1986).
[41] D. G. Dommermuth and D. K. P. Yue, A high-order spectral method for the study of nonlinear gravity waves, J. Fluid Mech. **184**, 267 (1987).
[42] G. Ducrozet, F. Bonnefoy, D. Le Touzé, and P. Ferrant, HOS-ocean: Open-source solver for nonlinear waves in open ocean based on High-Order Spectral method, Comput. Phys. Commun. **203**, 245 (2016).
[43] Y. Toda, F. Stern, and J. Longo, Mean-flow measurements in the boundary layer and wake and wave field of a Series 60 CB= 0.6 ship model—Part 1: Froude numbers 0.16 and 0.316, J. Ship Res. **36**, 360 (1992).

[44] H. Takeshi and T. Hino, Cooperative experiments on a series 60 model at Ship Research Institute-flow measurements and resistance tests, in *Proceedings of the 18th International Towing Tank Conference* (International Towing Tank Conference, 1987) pp. 10–13.
[45] M. S. Tarafder and K. Suzuki, Numerical calculation of free-surface potential flow around a ship using the modified Rankine source panel method, Ocean Eng. **35**, 536 (2008).
[46] I. Didenkulova, A. Sheremet, T. Torsvik, and T. Soomere, Characteristic properties of different vessel wake signals, J. Coastal Res. , 213 (2013).
[47] M. Li, Z. Yuan, and R. W. Yeung, Unsteady wave-making resistance of an accelerating ship, in *International Conference on Offshore Mechanics and Arctic Engineering*, Vol. 84379 (American Society of Mechanical Engineers, 2020) p. V06AT06A020.
[48] M. Rabaud and F. Moisy, Ship wakes: Kelvin or Mach angle?, Phys. Rev. Lett. **110**, 214503 (2013).
[49] K. Shi, Nonlinear large-scale ship wake patterns, 10.5281/zenodo.18344472 (2026).